Magnetism and magnetization dynamics in thin film ferromagnets

Verhagen, T.G.A.

CHAPTER 4

Sm-Co thin films

In this Chapter, we study the growth of Sm-Co thin films. They are of use as the strong ferromagnet in the ferromagnet/normal metal and ferromagnet/weak ferromagnet spin-flip laser. Sm-Co ferromagnets have the advantage that they have a large coercive field, which results in a wide magnetic field and frequency domain to test the spin-flip laser theory. In the literature, many groups have shown that thin Sm-Co films with a large coercive field can be grown using sputter deposition [93–99]. Furthermore, Sm-Co films have the advantage over bulk crystals that on top of the film in-situ an additional thin layer can be grown that can act for example as a protection layer against oxidation or as a spin-filter.

4.1 Sm-Co based magnetic materials

Modern permanent magnetic materials, like $SmCo_5$ or $Nd_2Fe_{14}B$, are based on intermetallic compounds of some rare-earth (RE) and 3d transition metals (TM). The materials are distinguished by high coercive fields caused by a high magnetocrystalline anisotropy with the easy magnetization direction along the c-axis of their hexagonal ($SmCo_5$) or tetragonal ($Nd_2Fe_{14}B$) structure.

The magnetic structure of Sm-Co binary systems is formed by Sm and Co sublattices that are both ferromagnetic [101, 102]. The magnetism in the Sm sublattice originates from the incompletely filled 4f electron shell of the Sm^{3+} ion (three electrons in 5d and 6s shells).

The 4f states are located deep in the atom, shielded by 5d and 6s electrons and therefore keep their localized character; the magnetism can be well described by the atomic characteristics of a free RE^{3+} ion using Hund's rules. The Co sublattice keeps its itinerant character with magnetic moment originating from the electron spin of the unpaired 3d electrons [103] of its $3d^6$ configuration.

In the RE-TM compounds, the spin moments of RE and TM are always aligned antiparallel. According to Hund's third rule, for electron shells that are filled less than half, the total angular momentum J forms as J = L - S, while for the shells filled more than half the total angular momentum forms as J = L + S. As a Sm^{3+} ion has 5 electrons in the 4f shell, the orbital angular momentum (L = 5) and spin angular momentum (S = $\frac{5}{2}$) are oriented opposite to each other (J = $\frac{5}{2}$). The total angular momentum for the Sm-sublattice is thus opposite to the spin angular momentum. The total magnetic momentum of the Sm-Co is the sum of the total magnetic moments of the Sm- and Co-sublattices, which are parallel aligned to each other and results in ferromagnetic behaviour.

The high uniaxial anisotropy is the result of the combined individual anisotropies of the Co and Sm sublattices, the Co-sublattice favors an uniaxial c-axis alignment, which is strengthened by the Sm sublattice that also favours c-axis alignment [103].

4.1.1 Phase diagram

The Sm-Co binary compounds have been intensively investigated since the 1970s, mainly for their exceptional magnetic properties [103]. Buschow [104] and Khan [105] systematically investigated the Sm-Co binary system when searching for new, improved permanent magnets. The phase diagram of the Sm-Co system is shown in Figure 4.1. In Table 4.1, crystal structure data and Curie temperatures are presented for all the reported compounds. One can see that the compounds with a high Curie temperature, important for making permanent magnets, are at the Co-rich side of the phase diagram: Sm_2Co_{17} (89.5 at % Co), $SmCo_5$ (83.3 at % Co), Sm_5Co_{19} (79.2 at % Co), Sm_2Co_7 (77.8 at % Co) and $SmCo_3$ (75.0 at % Co). All these compounds are incongruently melting materials structurally related to each other. Moreover, $SmCo_5$ is a metastable compound and Sm_2Co_{17} has two polymorphs. This brings difficulties with it in both single crystal and thin film growth of desired single-phase materials, as discussed later. From the structural point of view, the different Sm-Co phases can be derived from the $SmCo_5$-phase

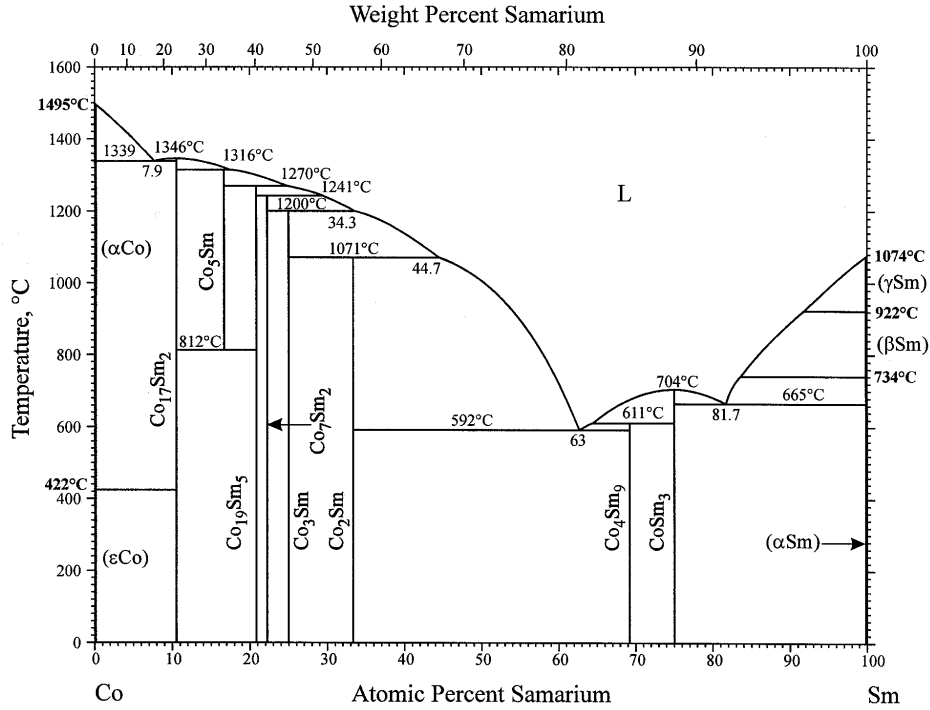

Figure 4.1: Sm-Co binary phase diagram [106]. Reprinted with kind permission from Springer Science and Business Media.

by substitution of a Co-atom by a Sm-atom or vice versa, followed by appropriate shifts of neighboring layers of atoms.

The unit cell of $SmCo_5$ is shown in Figure 4.2. In that cell, the Sm-atom is located at position (0, 0, 0) and the Co atoms are located at ($\frac{1}{3}$, $\frac{2}{3}$, 0), ($\frac{2}{3}$, $\frac{1}{3}$, 0), ($\frac{1}{2}$, 0, $\frac{1}{2}$), (0, $\frac{1}{2}$, $\frac{1}{2}$) and ($\frac{1}{2}$, $\frac{1}{2}$, $\frac{1}{2}$). Figure 4.3 shows how the Sm_2Co_7-unit cell can be obtained starting from the $SmCo_5$ lattice structure. In Figure 4.3.a several $SmCo_5$ unit cells are drawn, seen along the crystallographic b-direction. The first step to obtain Sm_2Co_7, is to replace in each third layer the Co-atom at position ($\frac{2}{3}$, $\frac{1}{3}$, 0) with a Sm-atom, as shown in Figure 4.3.b. The unit cell consists now of two $SmCo_5$ unit cells sandwiched between $SmCo_2$ unit cells, which makes the total unit cell three times as big. The substitution is followed by a shift of alternating unit cells by [$\frac{2}{3}$, $\frac{1}{3}$, 0] and a relaxation of the Sm-atoms that are too close to each other. This results in the Sm_2Co_7 unit cell, shown

Table 4.1: Crystal structure data [104, 108, 109] and Curie temperatures [110] for the different Sm-Co phases.

Compound	Space group	Crystal symmetry	Structure type	Lattice constants [Å]	T_{Curie} [°C]
α-Sm_2Co_{17}	$R\bar{3}m$	rhombohedral	Th_2Zn_{17}	a = 8.395 c = 12.216	> 400
β-Sm_2Co_{17}	$P6_3/mmc$	hexagonal	Th_2Ni_{17}	a = 8.360 c = 8.515	> 400
$SmCo_7$	$R\bar{3}m$	rhombohedral	Th_2Zn_{17}	a = 4.856 c = 4.081	> 400
$SmCo_5$	P6/mmm	hexagonal	$CaCu_5$	a = 4.982 c = 3.964	> 400
Sm_5Co_{19}	$R\bar{3}m$	rhombohedral	$Co_{19}Ce_5$	a = 5.031 c = 32.265	
Sm_2Co_7	$P6_3/mmc$	hexagonal	Ce_2Ni_7	a = 5.041 c = 24.327	20 - 400
$SmCo_3$	Pnma	rhombohedral	$GdZn_3$	a = 5.050 c = 24.950	20 - 400
$SmCo_2$	Fd3m	cubic	$MgCu_2$	a = 7.260	< 20
Sm_9Co_4		orthorombic	-	a = 11.15 b = 9.461 c = 9.173	< 20
Sm_3Co	Pnma	orthorombic	Fe_3C	a = 7.090 b = 9.625 c = 6.342	< 20

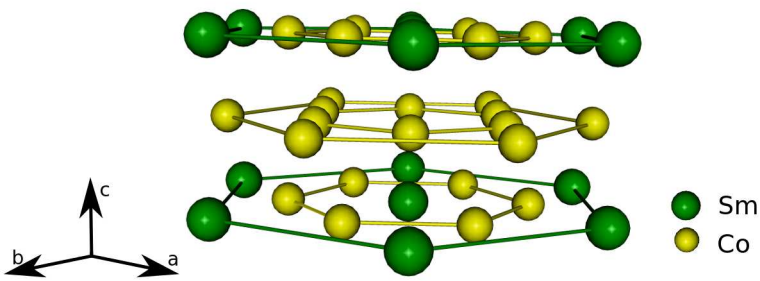

Figure 4.2: Lattice structure of $SmCo_5$. Image made with the program Molekel [107].

in Figure 4.2.c and d, which is six times as large as a $SmCo_5$ unit cell.

When replacing a Co atom with a Sm atom in each second layer instead of each third layer of $SmCo_5$, followed by the appropriate shift of neighboring layers, the result is the $SmCo_3$ phase. The substitution in each fourth layer would result in the Sm_5Co_{19} phase, with a hexagonal unit cell with a c-axis of 32 Å, and the substitution in each fifth layer would result in the $SmCo_4$-phase, with a hexagonal unit cell and a c-axis of 40 Å.

Another substitution scheme is the substitution of a Sm atom by pairs of Co atoms, which are usually called 'dumbbells'. In Figure 4.4.b, unit cells of $SmCo_5$ seen along the c-axis, are drawn with black lines. The Sm_2Co_{17}-phase is obtained from the $SmCo_5$-phase by replacing each third Sm-atom with a pair of Co-atoms. The unit cell of Sm_2Co_{17} is drawn with gray dotted line, where the replaced Sm atom is located at position A or B. The two Co-atoms substituted for the Sm atom are situated just above or below the basal plane of the unit cell. If the adjacent layers are stacked with the replaced Sm atom alternating at the A and B position, the hexagonal Sm_2Co_{17} is formed.

The $SmCo_7$ phase can be formed in a similar way, but now $\frac{2}{9}$ of the Sm atoms is replaced with a Co-pair.

The different Sm-Co phases are clearly closely related to each other and a small variation in the Sm concentration can result in different stacking "faults" which result in a different Sm-Co phase.

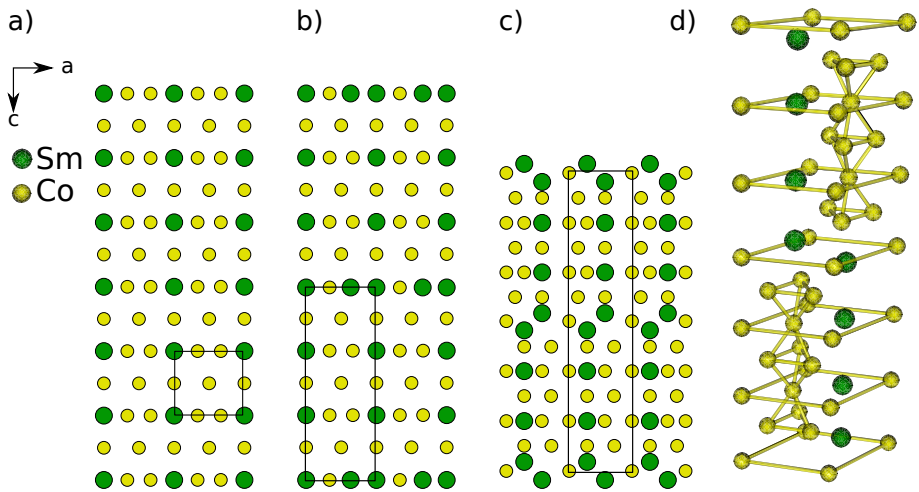

Figure 4.3: Construction of Sm_2Co_7 from $SmCo_5$. In a), the $SmCo_5$ structure is shown, projected along the b-axis. In every third unit cell, a Sm atom is substituted for a Co-atom, as shown in b), whereafter a block of two $SmCo_5$ unit cells sandwiched between $SmCo_2$ unit cells is shifted by $(\frac{2}{3}, \frac{1}{3}, 0)$, as can be seen in c). In d), the Sm_2Co_7 unit cell is shown. Image d) made with the program Molekel [107].

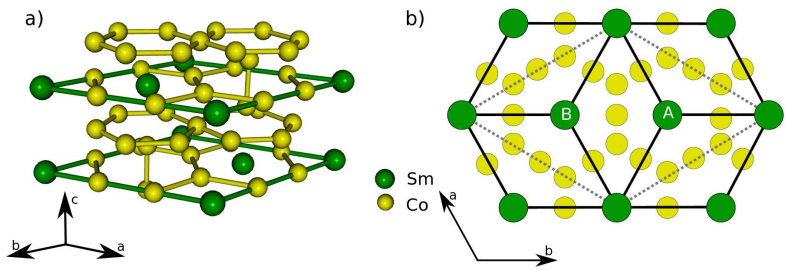

Figure 4.4: a) Structure of Sm_2Co_{17}, where in b) the atomic arrangement of a Sm sublattice in the basal plane in shown. The black lines indicate the $SmCo_5$ unit cell, where the gray dotted line indicates the Sm_2Co_{17} unit cell. Depending on the layer, a pair of Co atoms is at A and a Sm atom at B or vice versa. Image b) made with [107].

4.1.2 Sm-Co thin films

In the last years, recipes have been developed to grow films with the desired hard magnetic properties. One way to obtain them is to grow epitaxial thin films. Epitaxial growth can be obtained by using MgO(100), MgO(110) and Si(100) single crystal substrates, commonly in combination with a chromium buffer layer.

Sm-Co films can also be deposited on a glass substrate. Growing on glass results in very small crystallites in a disordered structure, but still yields large coercive fields [99].

Singh et al. [111] showed that growing Sm-Co films on the four-fold symmetric MgO(100) substrates results in the epitaxial relation Sm-Co(11$\bar{2}$0)[0001] // Cr(001)[110] // MgO(001)[100] (schematic diagram shown in Figure 4.5.a), where the Sm-Co grains are equally distributed along the two in-plane directions and the c-axis lies in the plane. Singh et al. [112] also showed that growing Sm-Co films on MgO(110) substrates results in the epitaxial relation Sm-Co(10$\bar{1}$0)[0001] // Cr(211)[0$\bar{1}$1] // MgO(110)[001]. Figure 4.5.b shows a schematic diagram how the Cr seed layer and hexagonal Sm-Co grows on MgO(100) and MgO(110).

Thin Sm-Co films are mostly grown using pulsed-laser deposition (PLD) [114–116] or sputter deposition [97–99] from single elemental targets Sm and Co. By tuning the sputter power of both sources or the pulse ratio by PLD, it is possible to grow compositions in the desired range. Sm-Co films can also be grown using sputter deposition [93–96] or PLD [117] from commercial alloy targets of $SmCo_5$.

One of the underlying problems of growing thin Sm-Co films, is the complexity of the Sm-Co phase diagram [106] which just has been discussed. The connection between composition and magnetic properties is therefore not trivial. Fortunately, high coercive fields can be found over a wide range of compositions and a number of studies [95, 98, 99] has focused on this particular aspect.

4.2 Experiment

The Sm-Co films in our experiment were deposited in a UHV chamber (base pressure 1×10^{-9} mbar) using DC magnetron sputter deposition with argon as plasma. Films were deposited on 500 μm thick MgO(100) and MgO(110) single crystal substrates on which a 100 nm thick Cr buffer layer was first deposited at 250°C in an Ar pressure of 1.5×10^{-3} mbar.

The Sm-Co films grown from a commercial $SmCo_5$ (3N) alloy target were approximately 100 nm thick and were grown at 450°C with an

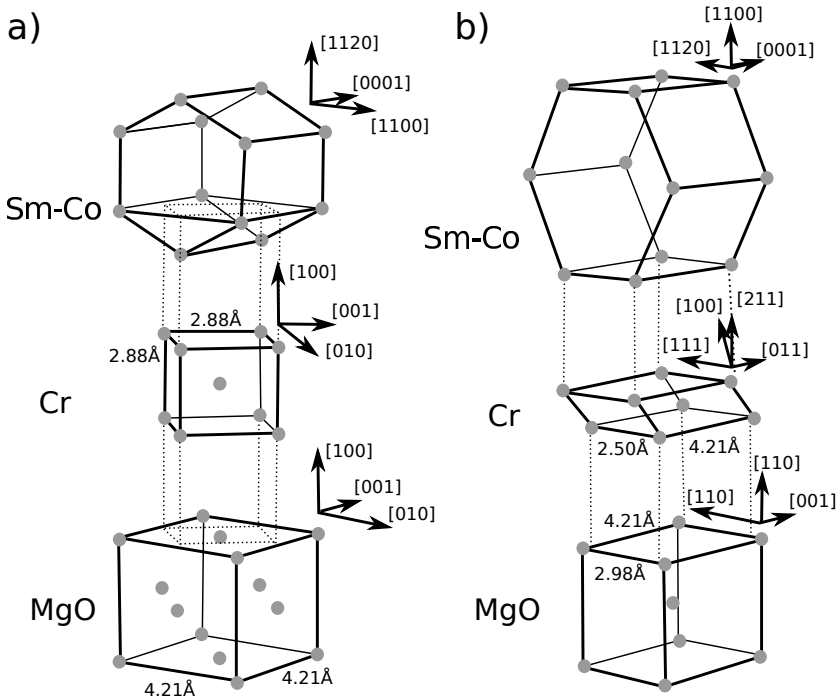

Figure 4.5: The unit cells (bold lines) and epitaxial relationships for the growth of a Cr buffer layer and a Sm-Co film on MgO(100) (a) and MgO(110) (b). Images adapted with permission from [113] © (1996), AIP Publishing LLC.

Ar pressure varying between 1.5×10^{-3} and 12.5×10^{-3} mbar and a deposition rate of approximately 4 nm/min. Afterwards, a 10 nm thick Cr layer was deposited at 450°C as a protection layer.

The Sm-Co films grown from single elemental Co (3N5) and Sm (3N) targets were approximately 100-140 nm thick and were grown with an argon pressure of 3.8×10^{-3} mbar at 450°C and a deposition rate of 3 nm/min. Afterwards, a 10 nm thick Cr or Cu layer was deposited at 100 °C as a protection layer. Different Sm-Co compositions were grown by varying the sputter power of the Co and Sm sources. The deposition rate is linear in the sputter current and 1 mA sputter current corresponds to approximately 0.2 Å/min for Co and 0.3 Å/min for Sm.

The deposition rate was measured by X-ray reflectivity (XRR) using Cu-Kα radiation and a rotating sample holder was used to obtain an uniform composition in the film.

The actual film composition and thickness were determined using Rutherford Backscattering (RBS). The structural quality of the film was measured with θ-2θ X-ray diffractometry (XRD) using Cu-Kα radiation, where the MgO substrate peak was measured as a reference for the angle, by using an extra Cu-absorber to decrease the intensity. The morphology of the films was characterized by Atomic Force Microscopy (AFM) in tapping mode. Magnetization measurements were performed in a SQUID-based magnetometer (MPMS 5S from Quantum Design) in fields up to 5 T. For the magnetization measurements, the substrates were cut in pieces of approximately 10×4 mm^2. As a reference, MgO(100) and Mgo(110) substrates were measured, and also an MgO(100) substrate with a 100 nm Cr film protected with 30 nm Cu. Electron paramagnetic resonance (EPR) spectra were measured at room temperature using a Bruker EMX plus X-band spectrometer in a TE_{011} cavity with 100 kHz modulation frequency and 1 G modulation amplitude.

4.3 Magnetic properties of Sm-Co thin films grown on MgO(100) deposited from a single alloy target

For various applications, growing Sm-Co thin films from alloy targets is a desirable option since only one deposition source is needed. Still, as far as we know, relatively few groups [93–96, 118–122] have reported on the growth of Sm-Co thin films from single alloy targets. The purpose of the next section is to show what the properties are of such films, grown on MgO(100), and in a range of pressures. In order to offer a reference frame for our results, we start with a paragraph outlining what has been achieved earlier in terms of coercive fields and saturation magnetization or remanence. We then present experimental details of our work, results of the measurements, and a discussion.

4.3.1 Single alloy targets; previous results

It is useful to compare results from single target growth to typical results from multiple targets. Without being exhaustive, PLD growth using multiple targets on Cr-buffered MgO(100) and MgO(110) was discussed by Singh *et al.* [114, 123]. In the first case, the more or less equal distribution of grain axes along the two in-plane directions leads to a remanent field $\mu_0 M_r$ of about 0.5 T when measuring along MgO(100),

as can be expected from the saturation magnetization $\mu_0 M_s$, which is about 1.1 T for $SmCo_5$. The room temperature coercive field $\mu_0 H_c$ was 2.4 T in this case. For growth on MgO(110) these numbers are $\mu_0 M_r$ = 0.9 T (due to a highly uniaxial grain distribution) and $\mu_0 H_c$ = 3 T, respectively. Sputter growth on Cr-buffered MgO(100) from multiple targets was performed, among others, by Fullerton et al. [124]. Using a pressure of 5×10^{-3} mbar, they reported square magnetization loops with $\mu_0 H_c$ = 3.4 T for a 30 nm film (decreasing to 1.2 T at 450 nm) but they did not give values for $\mu_0 M_s$ or $\mu_0 M_r$.

For single alloy targets, somewhat surprisingly, no work has been reported using MgO substrates, probably since coercive fields of the order of a Tesla do not require such a substrate. Also, a mixture of Co, Fe, Cu, and Zr was often used rather than pure Co in order to enhance coercivity. One parameter which did vary in the different studies is the sputtering pressure, which will be noted in units 10^{-3} mbar for easy comparison. A summary of the results, where we confine ourself to processes without post-annealing, is as follows.

Cadieu [93] reported on sputtering thin films using $Sm_2(Co,Fe,Zr,Cu)_{17}$ and $SmCo_5$ targets on Al_2O_3 substrates with a high sputter background pressure (80×10^{-3} mbar), so that the sputtered atoms were thermalized when they arrive onto the substrate and support the growth of large crystallites. For $SmCo_5$ he found $\mu_0 H_c$ = 2.4 T and $\mu_0 M_r$ = 0.9 T for a 3 μm thick film with a (110) texture. In a different publication [122] he showed that with a varying sputter gas pressure (between 20×10^{-3} mbar and 170×10^{-3} mbar) and different sputter gasses (Ar, Xe and ArXe), it is possible to vary the Sm concentration of the film from a Sm atomic percentage of about 12 atomic % to 16 atomic %. These films have a typical coercive field of 0.7 T and a remanent magnetization of 0.8 T.

Neu [94] et al. studied the Co-rich part of the Sm-Co phase diagram. Sm-(CoFeCuZr) films were grown by cosputtering $Sm(Co,Fe,Cu,Zr)_7$ and $SmCo_5$ targets on Al_2O_3 substrates. They varied the sputter background pressure in the range of 80 – 130 $\times 10^{-3}$ mbar. The magnetic properties of these Sm-Co films grown at a constant pressure show a smooth increase in the coercive field when the Sm concentration is increased from 15 atomic % to 18.5 atomic % (with 16.7 atomic % corresponding to $SmCo_5$). The remanent magnetization shows a smooth decrease, connected to the reduced amount of (Co,Fe). When the sputter background pressure is decreased from
110×10^{-3} mbar to 80×10^{-3} mbar, a clear increase in the coercive field and decrease in the remanent magnetization was observed, connected to a higher amount of Cu. The Sm(Co,Fe,Cu,Zr) film that contained 15.8 atomic % Sm and was grown at 80×10^{-3} mbar had a coercive

field of 0.7 T and a remanent magnetization of 0.8 T.

Speliotis and Niarchos [96] sputtered Sm-Co films on Si substrates from an alloy target with 18 atomic % Sm. They discussed the magnetic properties of the Sm-Co films, when the sputter background pressure was varied between 24×10^{-3} mbar and 32×10^{-3} mbar. Again, when increasing the Sm concentration from 11 atomic % to 17 atomic %, the remanent magnetization decreases and the coercive field increases. The Sm-Co film that contained 15 atomic % Sm had a coercive field of 1.5 T and a remanent magnetization of 0.7 T.

Summarizing, sputtering from single alloy targets has primarily been studied using Si or Al_2O_3 substrates under various conditions of pressure. The films typically show coercive fields of the order 0.7 T (and a maximum reported value of 2.4 T), and remanent fields of the order of 0.7 T – 0.8 T, as can be expected from the texturing. In our work we use a $SmCo_5$ alloy target and MgO(001) single crystal substrates with a Cr buffer layer, and grow films in an Ar pressure range between 1.5×10^{-3} and 12.5×10^{-3} mbar. We are able to vary the Sm content of the films with pressure between 15 atomic % Sm and 27 atomic % Sm. At room temperature we find typical values for $\mu_0 M_r$ of 0.4 T, somewhat lower than the above results; and values for $\mu_0 H_c$ up to 3.3 T, higher than reported until now.

4.3.2 Results

4.3.2.1 Composition and morphology

Figure 4.6.a shows the XRD scans of films grown at 1.5×10^{-3} mbar ($SmCo_5$-like) and 6.0×10^{-3} mbar (Sm_2Co_7-like) respectively. The observed peaks are labeled as reflections of Sm-Co, MgO and Cr. Due to the thickness and high crystallinity, also the K_β peak of the MgO substrate is visible. In Figure 4.6.b the region around the Sm-Co($11\bar{2}0$) peak is shown, for films grown with a sputter pressure of 1.5, 3.0, 6.0 and 9.0×10^{-3} mbar. Clearly visible is that, with decreasing pressure, the peaks shift to a higher angle. The measured lattice constant, determined from the Sm-Co($22\bar{4}0$) peak, and the Sm content, determined by RBS, are plotted in Figure 4.7 as a function of the sputter pressure. For films grown at a pressure above 6.0×10^{-3} mbar, the lattice parameter of the Sm-Co film is almost that of bulk Sm_2Co_7 (0.5040 nm). Decreasing the pressure from 6.0×10^{-3} mbar shows a decreasing lattice parameter, and at the lowest pressure the lattice constant of the Sm-Co film almost reaches the $SmCo_5$ bulk value (0.4982 nm). With re-

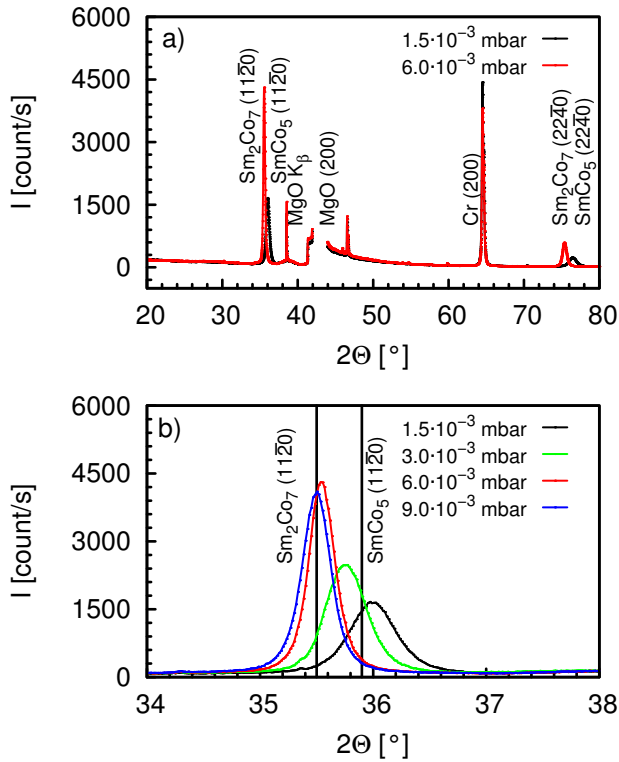

Figure 4.6: a) X-ray diffraction pattern (θ-2θ scan) of Sm-Co films grown from an Sm-Co alloy target on a Cr/MgO(100) substrate with two different sputter gas pressures, as indicated. b) shows the region around the Sm-Co(11$\bar{2}$0) peak, where the two vertical lines indicate the reflection of bulk crystalline Sm_2Co_7 (left) and $SmCo_5$ (right). Four samples are shown, grown at (from right lo left), 1.5 (black), 3.0 (green), 6.0 (red) and 9.0 $\times$ 10^{-3} mbar (blue).

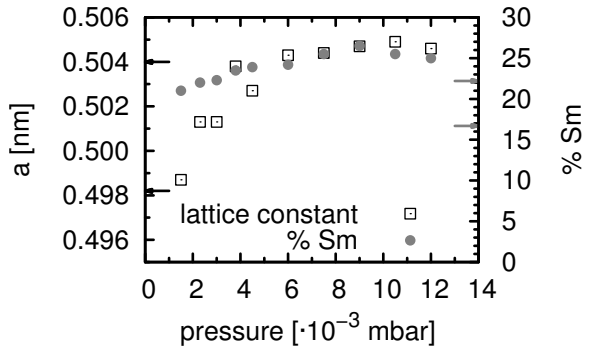

Figure 4.7: Lattice constant a of Sm-Co films and Sm concentration in the films as a function of the sputter background pressure, where the black ($\leftarrow$) and gray ($\rightarrow$) arrows indicate the lattice constant and Sm concentration of bulk $SmCo_5$ and Sm_2Co_7. Clearly visible is the change of the lattice parameter a from the Sm_2Co_7 phase (a = 0.5040 nm) to the $SmCo_5$ phase (a = 0.4982 nm).

spect to the Sm concentration, we consistently find a somewhat higher number than the stoichiometric Sm-Co phases would yield. Above 6.0×10^{-3} mbar, the Sm concentration is around 25 - 27 atomic % (compared to 22 atomic % for Sm_2Co_7). Below 6.0×10^{-3} mbar the Sm content gradually decreases to 21 atomic % (compared to 17 atomic % for $SmCo_5$).

Figure 4.8.a – d show the morphology of the Sm-Co films grown at 1.5, 3.0, 6.0 and 9.0×10^{-3} mbar, respectively. The films grown at a high sputter background pressures consist of rectangular grains with an average size of 70×250 nm^2, and with the long axis distributed over two orthogonal directions. Statistical analysis over an area of 1×1 μm^2 on the Sm-Co film grown at 6×10^{-3} mbar indicates an average surface roughness of 8.1 nm and a peak to peak value of 57 nm. When decreasing the pressure below 6×10^{-3} mbar, the shape of the grains slowly transforms from rectangular to square-like. Sm-Co films grown at 1.5×10^{-3} mbar consist of square grains with an average size of 75×75 nm^2. Statistical analysis over an area of 1×1 μm^2 on the Sm-Co film grown at 1.5×10^{-3} mbar indicates an average surface roughness of 9.6 nm and a peak to peak value of 55 nm.

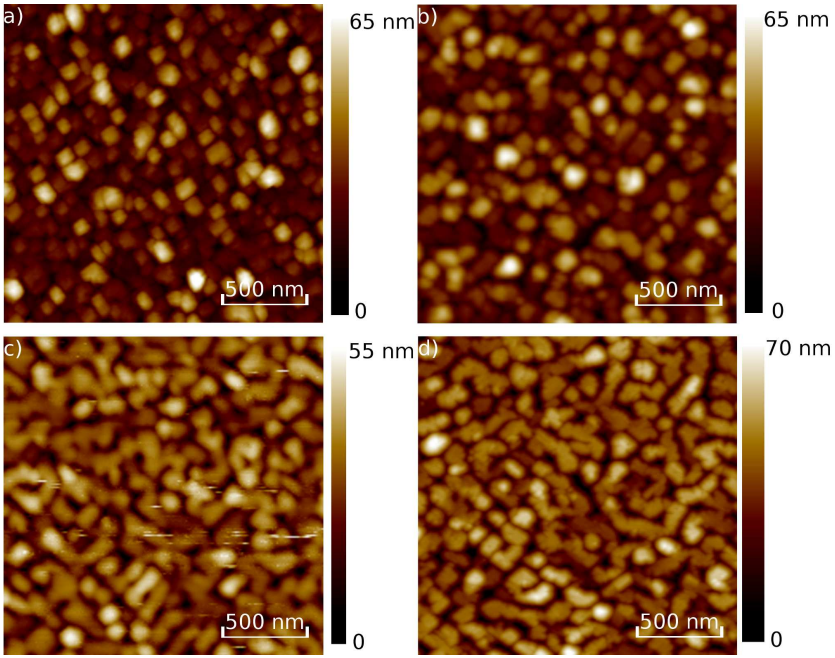

Figure 4.8: Morphology of Sm-Co films grown at a) 1.5×10^{-3}, b) 3×10^{-3}, c) 6×10^{-3} and d) 9.0×10^{-3} mbar measured with Atomic Force Microscopy.

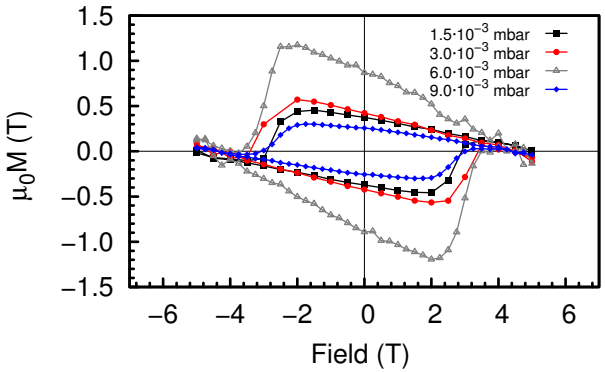

Figure 4.9: Magnetization $\mu_0 M$ as function of magnetic field at 300 K for Sm-Co films on a Cr/MgO(100) substrate grown with different sputter gas pressures as indicated.

4.3.2.2 Magnetic properties at room temperature

In Figure 4.9 the magnetization measurements are shown, taken at room temperature. The magnetization was calculated by dividing the measured magnetic moment by the measured volume of the Sm-Co films (typically 10 mm $\times$ 4 mm $\times$ 100 nm, where the Sm-Co thickness was determined using RBS). All samples show hysteretic behavior with a square-like loop and a large coercivity, of the order of 3 T, but also a substantial diamagnetic contribution. Separate measurements on an MgO(100) substrate and an MgO(100)/Cr(100 nm)/Cu(30 nm) film show that, at room temperature, the magnetic susceptibility χ of MgO for substrates from different batches varied and the samples measured had a magnetic susceptibility of - 2.4 and - 3.5 $\times$ 10^{-7} emu/g. These values are in agreement with χ = - 5.1 $\times$ 10^{-7} emu/g for a single crystal of MgO [125].

For the films grown at 1.5, 3.0 and 9.0 $\times$ 10^{-3} mbar, the coercive fields $\mu_0 H_c$ are 2.6, 3.0 and 2.6 T and the remanent magnetization $\mu_0 \mathrm{M_{rem}}$ are 0.4, 0.4 and 0.3 T. The film grown at 6.0 $\times$ 10^{-3} mbar has a coercive field of 3.0 T and a significantly larger remanent magnetization of 0.87 T. Both $\mu_0 \mathrm{H}_c$ and $\mu_0 \mathrm{M_{rem}}$ as a function of sputter pressure are given in Figure 4.10. Again we find clear trends: with increasing pressure up to 6 $\times$ 10^{-3} mbar $\mu_0 \mathrm{H}_c$ slowly increases from 2.6 T to 3.3 T, but above 6 $\times$ 10^{-3} mbar a rapid decrease sets in, down to 1.8 T at 12 $\times$ 10^{-3} mbar. The remanent magnetization is 0.42 T - 0.25 T in the whole pressure range, with the single exception of one film grown at 6.0 $\times$ 10^{-3} mbar, for which a value of 0.87 T is found. To characterize the magnetic texture, the ratio of the remanence of the in-plane and out-of-plane magnetization was determined for the films grown at 1.5 and 6.0 $\times$ 10^{-3} mbar (not shown). These data show that both films have a preferred in-plane orientation of the easy axis.

4.3.2.3 Target variability

One issue which came up during the research is target variability. We have grown Sm-Co films using a number of different commercially obtained targets with requested composition $SmCo_5$, which, according to the vendor, were fabricated from the same batch of alloy material. In Figure 4.11, the pressure dependence of the lattice constant of the Sm-Co films grown with three different targets is shown. The data discussed above were from films grown with target 1. Clearly visible is that the lattice parameters and therefore the exact film composition varies for the different targets. For target 2, the lattice parameters do not

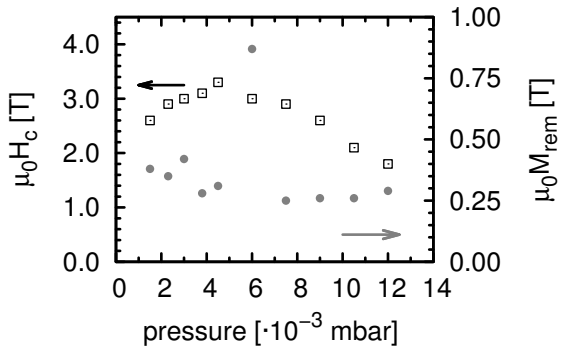

Figure 4.10: The coercive field $\mu_0 H_c$ and the remanent magnetization $\mu_0 M_{\text{rem}}$ at 300 K of the Sm-Co films as a function of the sputter background pressure.

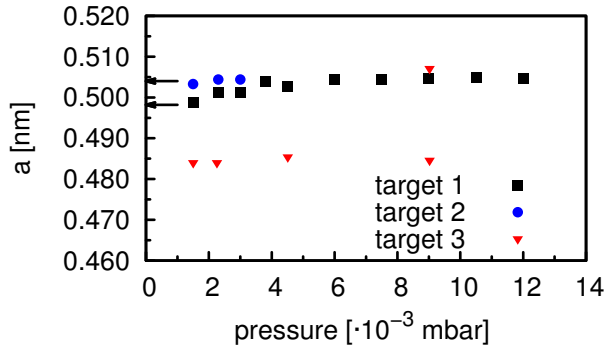

Figure 4.11: The lattice constant a of the Sm-Co films, grown with three different composite targets that were fabricated from the same batch of alloy material, as a function of the sputter background pressure. The black ($\leftarrow$) arrows indicate the lattice constant of bulk $SmCo_5$ and Sm_2Co_7. The two lattice constants at 9.0×10^{-3} mbar for target 3 indicates that there are two phases present in the film.

decrease when going to low pressure, which indicates a slight excess of Sm with respect to target 1. Films from target 3 show a considerably lower lattice parameter (typically 1 %) and apparently contain much more Co, although the lattice parameter is still lower than what is expected for the Sm_2Co_{17} compound (0.419 nm). The films grown with targets 2 and 3 showed coercive fields which were generally lower, between 1.0 and 2.0 T. We did not attempt to optimize the magnetic properties by varying the growth temperature.

4.3.2.4 Magnetic properties at low temperatures

We also investigated the low temperature behavior of the Sm-Co films. In Figure 4.12, the uncorrected magnetization hysteresis loops for a Sm-Co film grown at 10.5×10^{-3} mbar are shown as a function of temperature. For temperatures down to 30 K, the coercive field and the remanent magnetization increase slowly. Also, the diamagnetic contribution of the substrate becomes smaller. When going to even lower temperatures, the hysteresis loop shows a clear paramagnetic behavior. Figure 4.13.a shows magnetization measurements for two MgO substrates from different batches at 4 K, which are clearly paramagnetic in character. Electron paramagnetic resonance (EPR) measurements were done to identify the paramagnetic impurities. Figure 4.13.b shows the room temperature EPR measurements of a MgO substrate. Clearly visible are the resonance lines of Cr^{3+}, V^{2+} and Mn^{2+} impurities [126]. In Figure 4.14, the uncorrected and corrected magnetization hysteresis loops at 4.2 K for a Sm-Co film grown at 2.3×10^{-3} mbar are shown. For this measurement we added a Cu capping layer to the MgO/Cr film in order to preclude an unwanted contribution from oxidized Cr. Clearly visible is that the uncorrected loop is a minor loop, where the remanent magnetization for both the positive and negative field sweep has the same high and positive value. The magnetization hysteresis loop is corrected by subtracting the magnetization of the impurities. The corrected hysteresis loop is almost field independent, showing that the coercive field is larger than 5 T.

4.3.3 Discussion

Summarizing the experimental findings for target 1, we see that, when varying the sputter background pressure between 1.5×10^{-3} and 12.5×10^{-3} mbar, the Sm concentration in the films varies between 21 and 26.5 at%. In the whole pressure range, we find the Sm content of the films higher than expected from the stoichiometric ratio's of the line compounds. Appar-

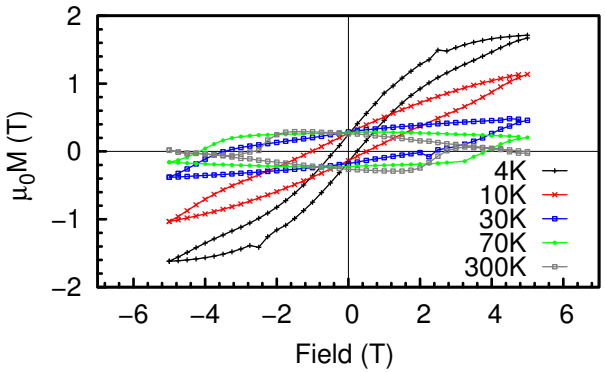

Figure 4.12: a) Magnetization $\mu_0 M$ as function of magnetic field of the Sm-Co film grown at 10.5 $\times$ 10^{-3} mbar as a function of temperature. For the 10 K and 4 K loop, the 5 T magnet of the magnetometer is not strong enough to reach the coercive field of the Sm-Co film while the contribution of the MgO substrate increases significantly.

ently, the sputter process does not result in a well-defined composition. In particular, the films are not a mixture of the $SmCo_5$ and Sm_2Co_7 compounds, which would result in two lines with different weight in the X-ray data. Rather, the films consist of one main composition which is able to incorporate a varying amount of Co-atoms. This is in line with the picture of Kahn [105], who proposed that the crystal structure of the intermetallic compounds can be seen as a one-dimensional superstructure of the $CaCu_5$-type structure, where in each i-th $CaCu_5$-type structure a Co-atom is replaced by a Sm-atom. Khan described this structure with the general formula $SmCo_y$, where y is equal to $(5n + 4)/(n + 2)$ (with n an integer). According to the XRD data, at the lowest pressure the films are close to the $SmCo_5$ compound, going to Sm_2Co_7 at higher pressures. With increasing sputter pressure, both the lattice constant and the value for $\mu_0 H_c$ increases until the pressure of 6.0 $\times$ 10^{-3} mbar is reached, where the lattice parameter corresponds to the Sm_2Co_7 alloy (although still with Sm excess). At the same time, $\mu_0 M_{\text{rem}}$ slowly decreases from about 0.4 T to 0.3 T. Increasing the pressure further, $\mu_0 H_c$ starts to decrease while $\mu_0 M_{\text{rem}}$ becomes constant. The surface morphology in Figure 4.8 shows that the grain size and grain shape changes when the sputter pressure is changed. At high pressures, relatively large rectangular grains are grown. When reducing the pressure,

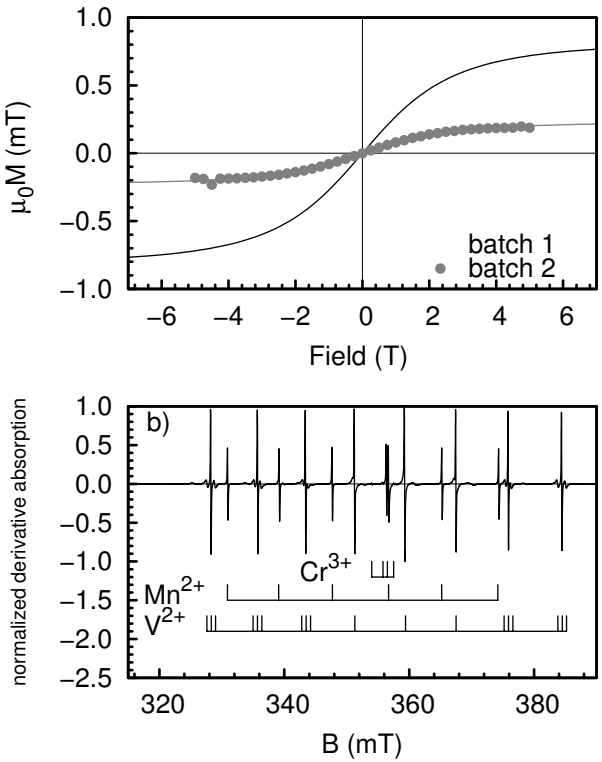

Figure 4.13: a) Magnetization $\mu_0 M$ as function of magnetic field for two MgO substrates from different batches measured at 4 K. The solid lines are fits to a Brillouin function using Cr^{3+}, Mn^{2+} and V^{2+} impurities. b) A typical room temperature EPR spectrum of a MgO single crystal substrate containing Cr^{3+}, Mn^{2+} and V^{2+} impurities.

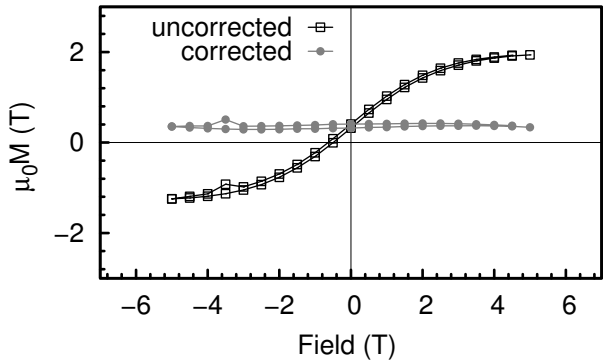

Figure 4.14: Magnetization $\mu_0 M$ as function of magnetic field (black squares) of the Sm-Co film grown at 2.3 $\times$ 10^{-3} mbar measured at 4.2K. The gray dots are the values for $\mu_0 M$ after correction for the substrate contribution. A small hysteresis characteristic of a minor loop is visible.

the grains become smaller and more square-like. We surmise this is due to the change in average energy of the atoms bombarding the substrate: at low pressure, this energy is higher and as a result, more defects are created during the growth of the first Sm-Co layers. When the number of defects becomes larger, also the number of preferred nucleation sites increases. The increase in the number of nucleation sites results in a reduced grain size and a more rough surface.
Connecting the structure/morphology data to the magnetization data, we see that in the range of pressures where the films change from $SmCo_5$-like to Sm_2Co_7-like, the values of $\mu_0 H_c$ (2.6 T – 3.3 T) and $\mu_0 M_{\rm rem}$ (0.4 T – 0.3 T) are the highest, and in particular $\mu_0 H_c$ is close to what has been achieved with cosputtering. $\mu_0 M_{\rm rem}$ is lower than optimal. For an equal distribution of two easy axes, the expected value is $\mu_0 M_s/\sqrt{2}$, or 0.78 T both for $SmCo_5$ and for Sm_2Co_7 [127]. This is in agreement with Ref. [115] where it was shown that excess of Sm leads to a significant decrease of $\mu_0 M_{\rm rem}$. The films grown above 6.0 $\times$ 10^{-3} mbar show a decrease in coercive field, although the Sm concentration, lattice constant and remanent magnetization do not change significantly with respect to the films grown at lower pressures. We attribute the change in coercive field to the larger grain size of the grown Sm-Co film. In experiments with nanoparticles with a different size, it was found that the size has a significant influence on the coercive field and a optimum particle size is approximately 100 – 200 nm [128]. The large remanent

magnetization of 0.87 T for the film grown at 6.0 $\times$ 10^{-3} mbar is an anomaly which is difficult to explain. In principle, either a strongly uniaxial texture could yield such a value close to the saturation magnetization, or a small grain size with strong exchange coupling between spins in the grain boundary area [129] but the morphology of the film does not point in such directions.

At low temperatures, the picture is somewhat complicated by the paramagnetic behavior of the MgO substrates, which is due to transition metal impurities, in particular Mn, V, and Cr. Their amount varies from batch to batch. Up to now, not much attention has been paid to the influence of the transition metal impurities on the properties of the grown films. Recently, the influence of the transition metal impurities on the optical and magnetic properties of a bare MgO substrate were studied [130]. Since the low temperature magnetic hysteresis shows a clear paramagnetic behavior superimposed on it, we assume that the magnetization $\mu_0 M_{\text{imp}}$ of these impurities can be described by the Brillouin function

$$\begin{aligned}\mu_0 M_{\text{imp}} = & NgJ\mu_B \frac{2J+1}{2J} \coth\left(\frac{2J+1}{2J}\frac{gJ\mu_B JB}{k_b T}\right) \\ & - NgJ\mu_B \frac{1}{2J} \coth\left(\frac{1}{2J}\frac{gJ\mu_B JB}{k_b T}\right)\end{aligned} \tag{4.1}$$

with N the number of atoms, g the g-factor, μ_B the Bohr magneton, J the total angular momentum, k_B Boltzman constant and T the temperature. The total magnetization for the three different impurities is then modeled as the sum of the magnetization of each type of impurities. From fitting equation 4.1 to the low temperature magnetization of a bare MgO substrate, we estimate that in the MgO substrates in Figure 4.13(a), the concentration of the impurities is in the range of 15–60 ppm [130]. When the contribution of the impurities in the MgO substrate is subtracted using equation 4.1, the Sm-Co film shows an almost constant magnetization as shown in Figure 4.14. The measured magnetic hysteresis loop is not the hysteresis loop itself, but a minor loop, since the coercive field is larger than the 5 T which can be reached in the magnetometer.

4.3.4 Conclusion sputtering single alloy target

When growing SmCo films from a single target with the nominal composition of $SmCo_5$ target on a Cr-buffered MgO(100) substrate, high

coercive fields can be reached, up to 3.3 T. In order to avoid low remanence, excess Sm has to be avoided. Although in principle the Sm content can be varied using the sputter pressure, the amount of control depends on the sputtering configuration. In the case described here, the lowest pressure at which we could grow films appears to be too high for this goal. A Co-rich target might be a solution for this problem. However, another difficulty we encountered was the high sensitivity of the film properties to different targets of nominally the same composition, which requires relatively costly optimization of the deposition conditions for each target separately. Targets with a composition closer to one of the line compounds in the phase diagram might be better suited to the purpose of single target sputtering, but this issue requires more research. At low temperatures we achieved the high coercive fields characteristic for these hard magnetic materials, but we also found that the data are strongly dominated by paramagnetic impurities in the MgO substrates.

4.4 Sm-Co thin films grown by cosputtering Sm and Co

The growth of Sm-Co thin films by sputter deposition from an alloy Sm-Co target looks an attractive way to grow thin films with a high coercive field and saturation magnetization. The big problem encountered above is the exact target composition. Our experience shows that with a target with the right composition very good films can be grown, but that a slight offset of the right composition changes the film properties dramatically. To overcome this problem, we also have grown films using sputter deposition from the single elemental targets Sm and Co.

Furthermore, growing Sm-Co films on MgO(100) substrates results in the epitaxial relation Sm-Co(11$\bar{2}$0)[0001] // Cr(001)[110] // MgO(001)[100], where in the film the Sm-Co grains are equally distributed along the two in-plane directions. This is not the ideal case for the fabrication of nanostructures, because it is unknown if the device is located at a grain where the magnetization is parallel or perpendicular to the grain. Therefore also the growth of Sm-Co thin films on MgO(110) substrates is studied. MgO(110) has the epitaxial relation Sm-Co(10$\bar{1}$0)[0001] // Cr(211)[0$\bar{1}$1] // MgO(110)[001]. In this way, all grains are oriented in the same direction.

In this section, it is shown that we can grow Sm-Co films by cosputtering from elemental Sm and Co targets. We also show that, when growing Sm-Co films on an MgO(100) substrate and varying the Sm concentration, we can grow films that can incorporate a varying amount

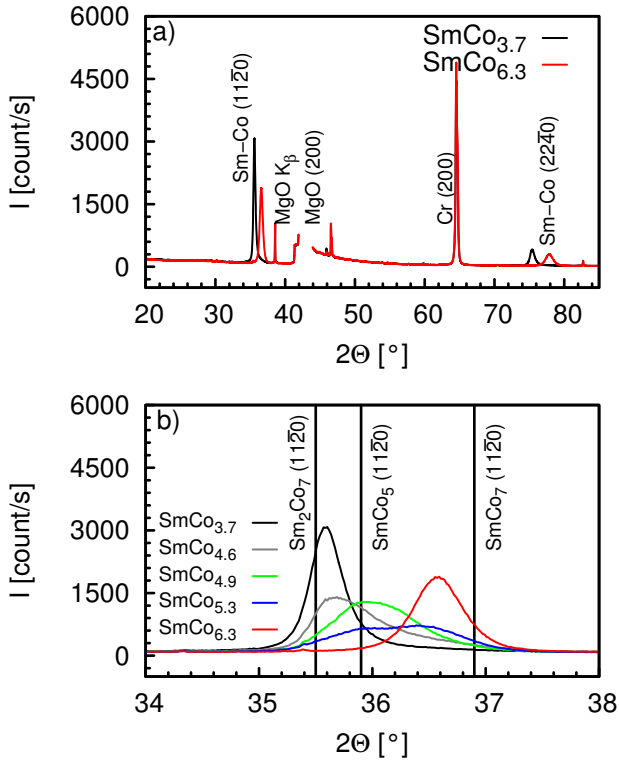

Figure 4.15: a) θ-2θ XRD scans of Sm-Co films grown by cosputtering from single elemental Sm and Co targets on a Cr/MgO(100) substrate with different levels of Sm sputter power and constant Co sputter power (except $SmCo_{5.3}$). b) shows the region around the Sm-Co(11$\bar{2}$0) peak, where the three vertical lines indicate the reflection of bulk crystalline Sm_2Co_7 (left), $SmCo_5$ (middle) and $SmCo_7$ (right). The nominal Sm/Co ratios are indicated.

of Co atoms. However, on an MgO(110) substrate we always grow multiple well-defined phases, where the Sm_2Co_7 and Sm_2Co_{17} phase are more easy to grow.

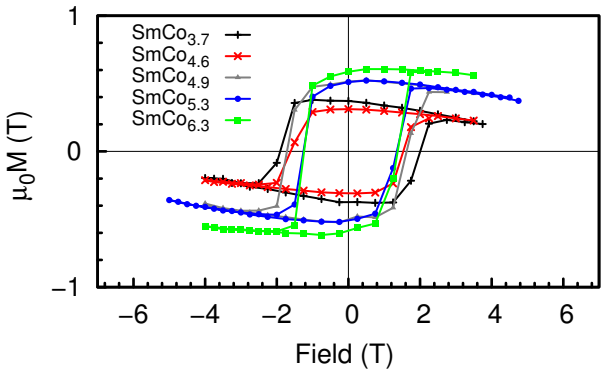

Figure 4.16: Uncorrected magnetic hysteresis of the Sm-Co films on a Cr/MgO(100) substrate grown with different Sm sputter powers at 300 K.

4.4.1 Results

4.4.1.1 Sm-Co films on MgO(100)

Figure 4.15.a shows the XRD scans of Sm-Co films grown on MgO(100) substrate with different compositions. The compositions have been changed by varying the Sm sputter power from 30 mA Sm ($SmCo_{6.3}$) up to 50 mA Sm ($SmCo_{3.7}$) and keeping the Co sputter power constant at 150 mA or 155 mA. The observed peaks are labeled as reflections of Sm-Co, Cr and MgO. Due to the thickness and high crystallinity, also the K_β peak of the MgO substrate is visible. In Figure 4.15.b, the region around the Sm-Co($11\bar{2}0$) peak is shown: $SmCo_{6.3}$ (30 mA Sm, 150 mA Co), $SmCo_{5.3}$ (37 mA Sm, 155 mA Co), $SmCo_{4.9}$ (37 mA Sm, 150 mA Co), $SmCo_{4.6}$ (40 mA Sm, 150 mA Co) and $SmCo_{3.7}$ (50 mA Sm, 150 mA Co). Clearly visible is that with an increasing Sm sputter current, the peak shifts to a smaller angle. Furthermore, for films with a Sm concentrations around 16 – 17%, the shape of the peak changes from a sharp single peak to a broad double peak.

In Figure 4.16, the uncorrected magnetization measurements are shown. The $SmCo_{3.7}$ and $SmCo_{4.6}$-films show a square-like loop with a coercive field $\mu_o H_c$ between 1.5 and 2.0 T and a remanent magnetization $\mu_0 M_{\text{rem}}$ between 0.33 and 0.45 T. The $SmCo_{4.9}$, $SmCo_{5.3}$ and $SmCo_{6.3}$ films have a more rounded hysteresis loop with lower coercive fields than the Sm-rich films, but $\mu_0 M_{\text{rem}}$ is larger than the Sm-rich films. Both $\mu_0 M_{\text{rem}}$ and $\mu_o H_c$ are plotted as a function of the Sm con-

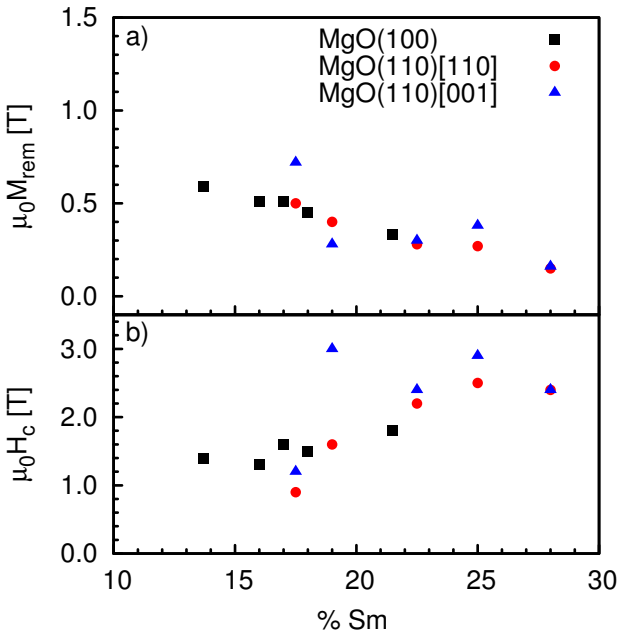

Figure 4.17: The remanent magnetization $\mu_0 M_{\text{rem}}$ (a) and the coercive field $\mu_o H_c$ (b) of the Sm-Co films on MgO(100) (black ■) and MgO(110) substrates for different Sm concentrations. The field is oriented in the film plane in all cases, and along the [110]-direction (red ●) and [001]-direction (blue ▲) for the MgO(110) substrates.

centration in Figure 4.17. With increasing Sm content, $\mu_o H_c$ becomes larger, but $\mu_0 M_{\text{rem}}$ decreases smoothly.

Figure 4.18 shows the morphology of the Sm-Co films. The $SmCo_{4.6}$ (a) and $SmCo_{4.9}$ (b) film consist of rectangular grains. When increasing the Sm concentration, the $SmCo_{5.3}$ film consists of clusters of small round grains and the $SmCo_6$-film becomes a very smooth, roughness is 2 nm, almost closed film, where no grains are visible.

4.4.1.2 Sm-Co films on MgO(110)

In Figure 4.19, the XRD scan of Sm-Co films grown on MgO(110)/Cr substrates with a different Sm concentration are shown. The compositions have been changed by varying the Co sputter rate from 115 mA ($SmCo_{2.6}$) up to 190 mA Co ($SmCo_{4.7}$) and keeping the Sm sputter

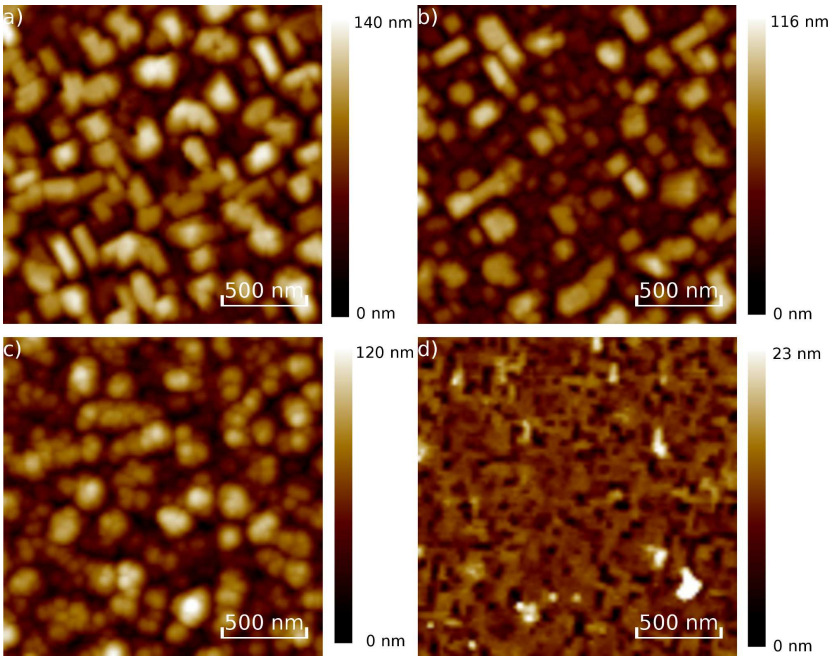

Figure 4.18: Morphology of the Sm-Co films grown on MgO(100) measured with atomic force microscopy, where a) is a $SmCo_{4.6}$ film with a roughness of 19 nm, b) is a $SmCo_{4.9}$ film with a roughness of 16 nm, c) is a $SmCo_{5.3}$ film with a roughness of 13 nm and d) is a $SmCo_{6.3}$ film with a roughness of 2 nm.

rate constant at 50 mA. The observed peaks are labeled as reflections of Sm-Co, Cr and MgO. Whereas the Cr layer on MgO(100) grows as the cubic (100) phase, on MgO(110) Cr grows as the monoclinic Cr(211) phase. Figure 4.19.b shows the region around the Sm-Co(200) peak, for Sm-Co films with a different composition: $SmCo_{2.6}$ (115 mA Co), $SmCo_{3.0}$(130 mA Co), $SmCo_{3.4}$ (145 mA Co), $SmCo_{4.3}$(175 mA Co) and $SmCo_{4.7}$(190 mA Co). Clearly visible, is that all the films show diffraction peaks at the Sm_2Co_7, $SmCo_5$ and Sm_2Co_{17} phases. The $SmCo_{2.6}$ film consists mainly of the Sm_2Co_7 phase and a small amount of the $SmCo_5$ phase. When increasing the Co concentration, the Sm_2Co_7 and the $SmCo_5$ phase in the film diminishes and the $SmCo_7$ or Sm_2Co_{17} phase becomes the dominant phase in the film.

In Figure 4.20, the uncorrected magnetization measurements of the

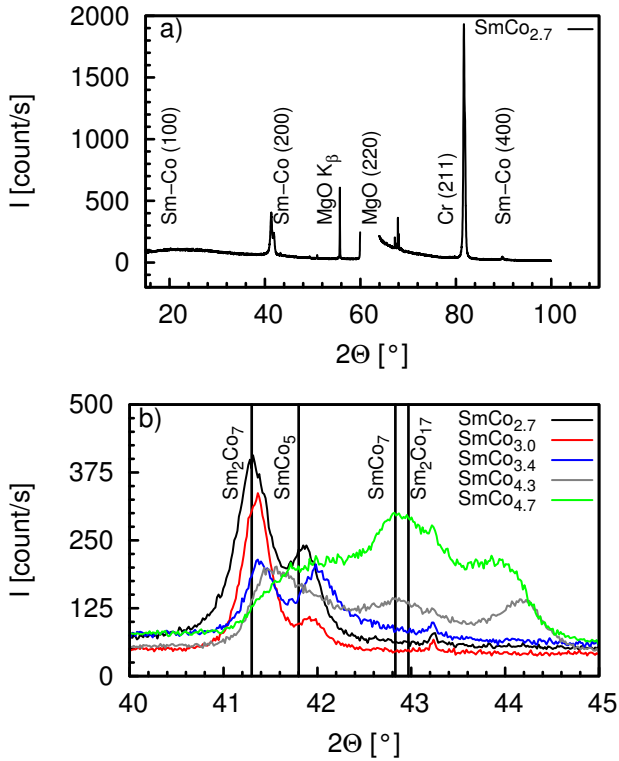

Figure 4.19: θ-2θ XRD scans of Sm-Co films grown by cosputtering from single elemental Sm and Co targets on a Cr/MgO(110) substrate with different sputter power levels. b) shows the region around the Sm-Co(200) peak, where the three vertical lines indicate the reflections for bulk crystalline Sm_2Co_7 (left), $SmCo_5$ (middle left), $SmCo_7$ (middle right) and Sm_2Co_{17} (right).

Sm-Co films on MgO(110) are shown. The $SmCo_{4.7}$ film has a large remanent magnetization of 0.50 T in the MgO[110]-direction and a remanent magnetization of 0.72 T in the MgO[001]-direction. With an increasing Sm concentration, the remanent magnetization decreases in both the [110] and [001]-direction. The coercive field behaves in the opposite way. The $SmCo_{4.7}$ film has a coercive field of 0.9 T in the MgO[110]-direction and 1.2 T in the MgO[001]-direction. With an increasing Sm concentration, the coercive field increases in both directions, as can be seen clearly in Figures 4.17 and 4.20.

The morphology of the Sm-Co films grown on MgO(110) is shown in Figure 4.21. The crystal structure looks quite different from the morphology of the Sm-Co films grown on MgO(100). While the films on MgO(100) grow as big crystallites for the Sm-rich films, on MgO(110) it looks as if the crystallites are grouped as rows of small grains, as is clearly visible in Figure 4.21.a. When increasing the Co concentration, the grains in the rows become larger and there are less grains in a row. For the $SmCo_{4.7}$ film, the grains becomes smaller again and there are more grains in a row.

4.4.2 Discussion

4.4.2.1 Sm-Co films on MgO(100)

When varying the sputter current, the composition and phase of the Sm-Co thin films on MgO(100)/Cr can be controlled as is shown in Figure 4.15. The composition can be varied more or less continuously and the XRD scans show the high sensitivity to changes of the sputter rate. The optimum $SmCo_5$ films are grown with a Sm source current of 37 mA, while a difference of 1 mA (0.05 nm/min or 2-3 % Sm) is already clearly visible. When increasing the Sm concentration by increasing the Sm source current, the Sm_2Co_7 and $SmCo_5$ phases are both grown, as can be seen from the two peaks in the XRD scan. This growth behaviour is different from the growth from an alloy target, which tends to form either the Sm_2Co_7 or the $SmCo_5$ phase, as was shown in Section 4.3. When increasing the Sm concentration even further, single phase Sm_2Co_7 films can be grown at 50 mA Sm sputter current.

Still, the magnetic properties of the Sm-Co films on MgO(100) show the expected behaviour. Co-rich films have a smaller coercive field, but a larger remanent magnetization. When increasing the Sm concentration, $\mu_0 M_{\text{rem}}$ becomes smaller and $\mu_o H_c$ becomes larger. However, the Sm-Co films do not show the really large coercive fields that can be expected for this type of films. The main difference between the films

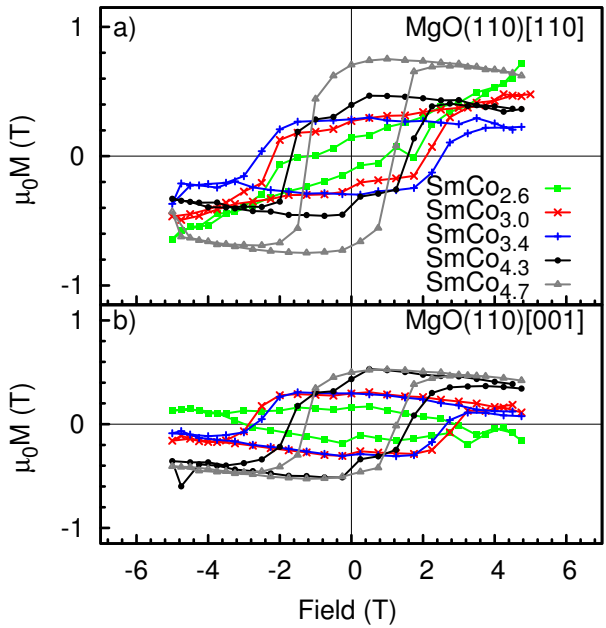

Figure 4.20: Uncorrected magnetic hysteresis of the Sm-Co films on a Cr/MgO(110) substrate with the field applied in the MgO(110)[110] (a) and MgO(110)[001] (b) direction, grown with different Co sputter powers levels at 300K.

grown using sputter deposition from an alloy target and cosputtering is the size of the Sm-Co grains. It has been recently shown that the grain size significantly affects the coercivity [128]. In Figure 4.8, atomic force microscopy images show that the grains of the Sm-Co films grown from the alloy target are much bigger than the grains from the Sm-Co films grown by cosputtering. Furthermore, a constant sputter gas pressure was used for the cosputter growth of the Sm-Co films, while the sputter gas pressure is an important parameter for the growth of Sm-Co films, as was shown in Section 4.3.

4.4.2.2 Sm-Co films on MgO(110)

The XRD scans of the films on grown on MgO(110) are more complicated. Always a mixture of the Sm_2Co_7, Sm_2Co_{17}, $SmCo_5$ and/or $SmCo_7$ phases is grown. From the Sm-Co phase diagram, it is clear that

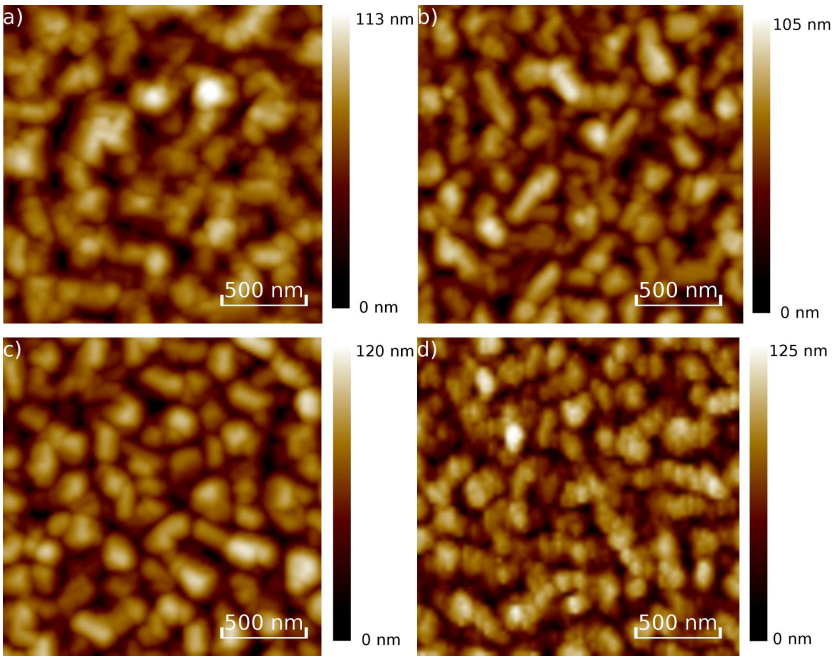

Figure 4.21: Morphology of the Sm-Co films grown on MgO(110) measured with atomic force microscopy, a) is a $SmCo_{3.0}$ film with a roughness of 16 nm, b) is a $SmCo_{3.4}$ film with a roughness of 18 nm, c) is a $SmCo_{4.3}$ film with a roughness of 19 nm and d) is a $SmCo_{4.7}$ film with a roughness of 19 nm.

$SmCo_5$ is not a stable line compound, and it lies close to two other alloys; Sm_2Co_7 on the Sm-rich side and $SmCo_7$ on the Sm-poor side. Apparently, the growth process on this surface is very delicate and does not easily result in a well-defined single phase; minor changes in composition change the growth significantly.

The magnetic properties of the grown Sm-Co films on MgO(110) show a large coercive field at room temperature. Values $\mu_0 M_{\mathrm{rem}}$ and $\mu_o H_c$ as a function of the Sm concentration, as shown in Figure 4.17, show the expected behaviour. However, the magnetization measurements along the MgO(110)[110], do not show the expected hard axis behaviour, which indicates that the film does not grow only along the expected MgO[001] axis. This is also visible in the surface morphology, as shown in Figure 4.21. The grains appear randomly distributed on

the surface and are not aligned in one direction.

For the growth of the Sm-Co films on the MgO(110) substrates, the same temperature and constant Ar background sputter pressures was used for the growth of the Sm-Co films on the MgO(100) substrates. We expect that the growth of a single phase Sm-Co film with an easy axis along the MgO[001] direction, would be very sensitive to the exact growth parameters like temperature and sputter gas pressure.

To conclude, by varying the sputter current of the Sm and/or Co target, we can change the phase for the Sm-Co alloy from a $SmCo_5$-like to the Sm_2Co_7-like phase, when the film is grown on MgO(100). When the Sm-Co film is grown on MgO(110), the Sm-Co film consists of multiple phases where the amount of each phase depends on the sputter power. We find that the film composition is extremely sensitive to small variation in sputterpower levels. The films grown on MgO(100) and MgO(110) have good magnetic properties, but the crystal texture of the films on MgO(110) does not show the expected two-fold symmetry.